Chemical Science

ROYAL SOCIETY OF CHEMISTRY

EDGE ARTICLE

View Article Online
View Journal | View Issue

Cite this: *Chem. Sci.*, 2025, **16**, 15666

All publication charges for this article have been paid for by the Royal Society of Chemistry

Received 3rd June 2025
Accepted 25th July 2025

DOI: 10.1039/d5sc04035c

rsc.li/chemical-science

Brønsted bases promote interfacial proton transfer for enhanced biomass electrocatalysis

Jia Wu, Jianlong Zhang, Zhixiang Zhai, Zelong Sun, Zhangyue Zheng, Junxin Chen, Zihui Ning, Huan Wen* and Shibin Yin *

Efficient electrooxidation of 5-hydroxymethylfurfural (HMF) is essential for the production of valuable chemicals from biomass. However, the sluggish interfacial proton transfer kinetics during the reaction significantly hinder its progress. This study proposes that the introduction of Brønsted bases on cobalt-based catalysts can enhance HMF oxidation by modulating interfacial proton transfer kinetics. Density functional theory calculations, *in situ* spectroscopy, and experimental results demonstrate that phosphate (Pi) groups on the cobalt surface shorten the distance between the proton donor and acceptor, effectively promoting interfacial proton transfer during the dehydrogenation of HMF. Consequently, the Pi-functionalized catalyst shows a 6.5-fold increase in current density compared with the unmodified cobalt catalyst and achieves near 100% selectivity for 2,5-furandicarboxylic acid, attaining a current density of 1000 mA cm^{-2} at 1.41 V_{RHE} for efficient HMFOR. This work provides insights into designing efficient catalysts for industrial applications through surface site functionalization.

Introduction

Electrocatalytic refineries offer a promising alternative to traditional fossil fuel-based refineries, enabling the conversion of biomass feedstocks into valuable fuels and chemicals.[1–3] 5-Hydroxymethylfurfural electrooxidation reaction (HMFOR) is a green route to produce high-value biomass-derived chemicals and has garnered significant attention.[4,5] The development of efficient nonprecious metal catalysts is crucial for increasing catalytic efficiency.[6–15] Cobalt-based catalysts have attracted considerable attention owing to their favorable onset potential, but their limited electron–proton transfer capacity hinders reaction rates and product selectivity for the electrooxidation of 5-hydroxymethylfurfural (HMF) to 2,5-furandicarboxylic acid (FDCA).[16] To address these limitations, strategically modifying the properties of cobalt-based materials and elucidating their catalytic mechanisms are essential.

HMFOR occurs at the catalyst surface or interface through a dehydrogenation process involving the activation and break of C–H/O–H bonds and associated electron–proton transfer processes.[17–19] Specifically, the catalyst (acting as a proton acceptor) facilitates proton transfer from the reactant molecules (proton donor) to the product side *via* the transition state, with associated electron transfer stabilizing the process,[20] as illustrated in Fig. 1a. Owing to the significant kinetic disparity in transport between electrons and protons, electron transfer is generally faster than proton transfer, making the latter the rate-determining step (RDS).[18,19] Consequently, understanding and optimizing the interfacial proton transfer kinetics is crucial for developing highly efficient HMFOR catalysts.

The kinetic core of the proton transfer process fundamentally depends on the overlap of the vibrational wave functions of the proton donor and acceptor, which is a quantum mechanical phenomenon that controls the probability of proton tunneling.[21,22] The increase in the binding strength between the proton donor and acceptor leads to a shortness of the distance, which significantly increases the wave function overlap and enhances the proton tunneling effect, thereby reducing the proton transfer energy barrier and promoting the break of the chemical bond.[22] According to Brønsted–Lowry acid–base theory, a Brønsted base can act as an effective proton acceptor by combining with proton to form conjugate acid, which is a process governed by its pK_a value.[23] Among various Brønsted base groups, the phosphate (PO_4^{3-}, denoted as Pi) group, with its high pK_a value,[24,25] is particularly attractive for promoting rapid proton transfer kinetics during HMFOR processes.

Inspired by this idea, this work proposes a strategy to regulate the interfacial proton transfer kinetics over cobalt nanowires through Brønsted base (Pi) functionalization (Fig. 1b). Density functional theory (DFT) simulations and experimental approaches confirm that the functionalized Pi group provides additional equivalent hydrogen sites that act as effective carriers for proton transfer, shortening the distance between the proton donor (HMF) and acceptor (Pi-Co) and increasing the overlap of their proton vibration wave functions. This facilitates proton transfer from the reaction molecules to the catalyst

Guangxi Key Laboratory of Electrochemical Energy Materials, School of Chemistry and Chemical Engineering, Guangxi University, 100 Daxue Road, Nanning 530004, China. E-mail: wenhuan@gxu.edu.cn; yinshibin@gxu.edu.cn

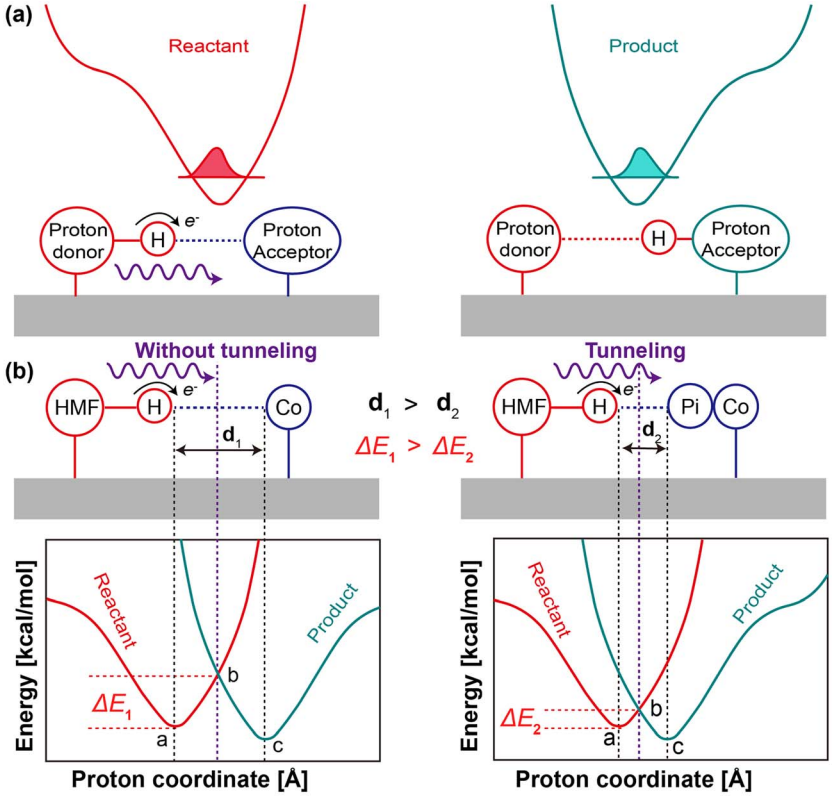

Fig. 1 (a) Schematic diagram of hydrogen proton transfer at the catalyst interface. The red and cyan curves represent the proton potential and proton wave function (shaded curve) in the ground state of the reactant and product, respectively, which are functions of proton coordinates; (b) schematic diagram of the proton coordination and proton transfer energy barriers between the proton donor (HMF) and the acceptors (Co and Pi-Co).

surface, reducing the energy barrier for the dehydrogenation of the RDS and thereby improving the kinetics and selectivity of HMFOR. Consequently, the Pi-functionalized catalyst shows a 6.5-fold increase in current density compared with the unmodified cobalt catalyst and achieves near 100% selectivity for FDCA, attaining a current density of 1000 mA cm^{-2} at 1.41 V_{RHE} for efficient HMFOR.

Results and discussion

As shown schematically in Fig. 2a, a Co nanowire precursor is grown on nickel foam (NF) through a simple hydrothermal treatment (Fig. 2b). Subsequently, it undergoes phosphating treatment and cyclic voltammetry activation to obtain catalysts functionalized with Pi groups. The obtained catalyst with a Pi content of 2.77 mmol% is determined by ion chromatography (Fig. 2c and S1). The Co sample is prepared for comparison. Scanning electron microscopy (SEM) images show that both the Co and Pi-Co samples exhibit nanowire morphologies (Fig. S2). X-ray diffraction (XRD) patterns indicate that the composition of Pi-Co is similar to that of metallic Co (PDF #05-0727; #15-0806) (Fig. 2d), suggesting that the structure of metallic Co is well preserved, even after phosphating treatment. Furthermore, transmission electron microscopy (TEM) reveals an amorphous region with a thickness of 2–4 nm on the nanowire surface (Fig. 2e), which may be attributed to the introduction of Pi groups. The lattice fringes with interplanar spacings of 0.204 nm and 0.217 nm are indexed to the (111) and (100) planes of metallic Co (Fig. 2e and f), respectively. Energy-dispersive X-ray mapping images demonstrate the presence of Co, P, and O in the catalyst (Fig. S3).

X-ray photoelectron spectroscopy (XPS) is performed to study the chemical properties of the samples.[26] The XPS survey spectrum confirms the presence of Co, P, and O in Pi-Co (Fig. S4). The Co 2p spectra are deconvoluted into two peaks corresponding to Co^0 (778.0/793.4 eV) and Co^{2+} (781.1/796.5 eV) (Fig. 2g), respectively, and the oxidation state is attributed to the inevitable surface oxidation.[10,27] Compared with that of the Co sample, the intensity of the Co^0 peak is lower because of the introduction of Pi groups on the Co surfaces. The appearance of a P $2p_{3/2}$ peak (133.6 eV) and a P $2p_{1/2}$ peak (134.4 eV) in the P 2p spectra corresponds to PO_4^{3-} (Fig. S5a).[28] Notably, the PO_4^{3-} ligand has a strong coordination effect and can form P–O–M bonds with metal sites, which is confirmed by the P–O–Co linkage (531.2 eV) of O 1s spectra (Fig. S5b) and the P–O–Co vibrations (1055 cm^{-1}) of Fourier transform infrared spectroscopy (FTIR) (Fig. S6).[29,30] Furthermore, the chemical composition of the catalyst at different depths is examined *via* XPS in conjunction with Ar^+ sputtering. Fig. 2h–j shows that the peak intensity of Co^0 in the Co 2p spectra notably increases with an

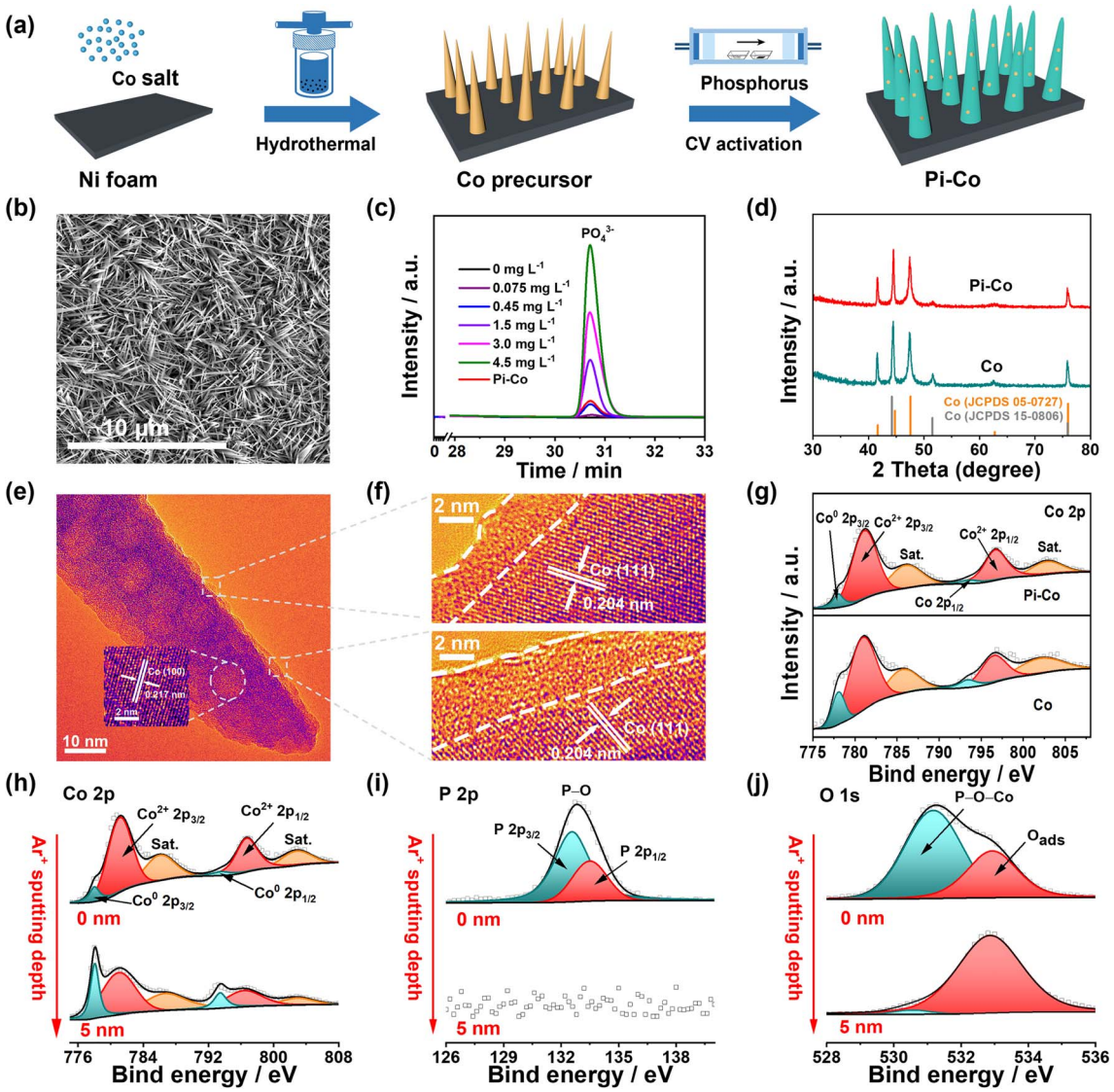

Fig. 2 (a) Schematic illustration of the synthetic route of the Pi-Co catalyst; (b) SEM image of the Co precursor nanowire; (c) ion chromatography for different concentrations of PO_4^{3-} and Pi-Co catalyst; (d) XRD patterns of the Pi-Co and Co catalysts; (e and f) TEM and HRTEM images of Pi-Co catalyst; (g) Co 2p XPS spectra of Pi-Co and Co catalysts; XPS depth profile for (h) Co 2p, (i) P 2p and (j) O 1s of Pi-Co catalyst.

Ar^+ sputtering depth of 5 nm. Conversely, the peak intensities of PO_4^{3-} and P–O–Co linkages in the P 2p and O 1s spectra almost disappear. By combining the above results, it can be inferred that the Pi groups are successfully functionalized on the Co nanowires surface.

The electrocatalytic study of HMFOR is then performed in a three-electrode electrolyzer with 1.0 M KOH/50 mM HMF. Compared with the Pi-Co and Co samples, the contribution of bare NF to the electrocatalytic activity is negligible and will not be discussed later (Fig. 3a). Pi-Co catalyst only needs a small potential of 1.08/1.16/1.41 V_{RHE} to reach a current density of 10/100/1000 mA cm^{-2}, respectively, which is significantly lower than that of the Co sample (1.17/1.36/1.65 V_{RHE}) and competitive with the reported catalysts (Fig. 3b and Table S1).[31–38] Notably, the current density of Pi-Co is 6.5 times that of Co catalyst at 1.40 V_{RHE} (Fig. 3c), confirming that the functionalization of Pi is beneficial for HMFOR. Additionally, the HMFOR LSV curves are normalized by the electrochemical surface area (ECSA), which is determined by the double-layer capacitance (C_{dl}) method, and the results indicate the better intrinsic activity of Pi-Co than that of Co sample (Fig. S7).

During the electrooxidation process of HMF, the OER emerges as the primary competitive reaction. Therefore, a comparative analysis of the HMFOR and OER processes is conducted. Fig. S8 shows that the addition of 50 mM HMF results in a substantially lower onset potential and a higher current density compared to 1.0 M KOH, demonstrating that the oxidation of HMF is dominant, while OER occurs at more positive potentials than 1.45 V_{RHE}. Subsequently, the HMF conversion tests are conducted in the potential of 1.25 to 1.45 V_{RHE} over the Pi-Co catalyst. The results indicate that 1.35 V_{RHE} is appropriate for electrooxidizing HMF to FDCA since it

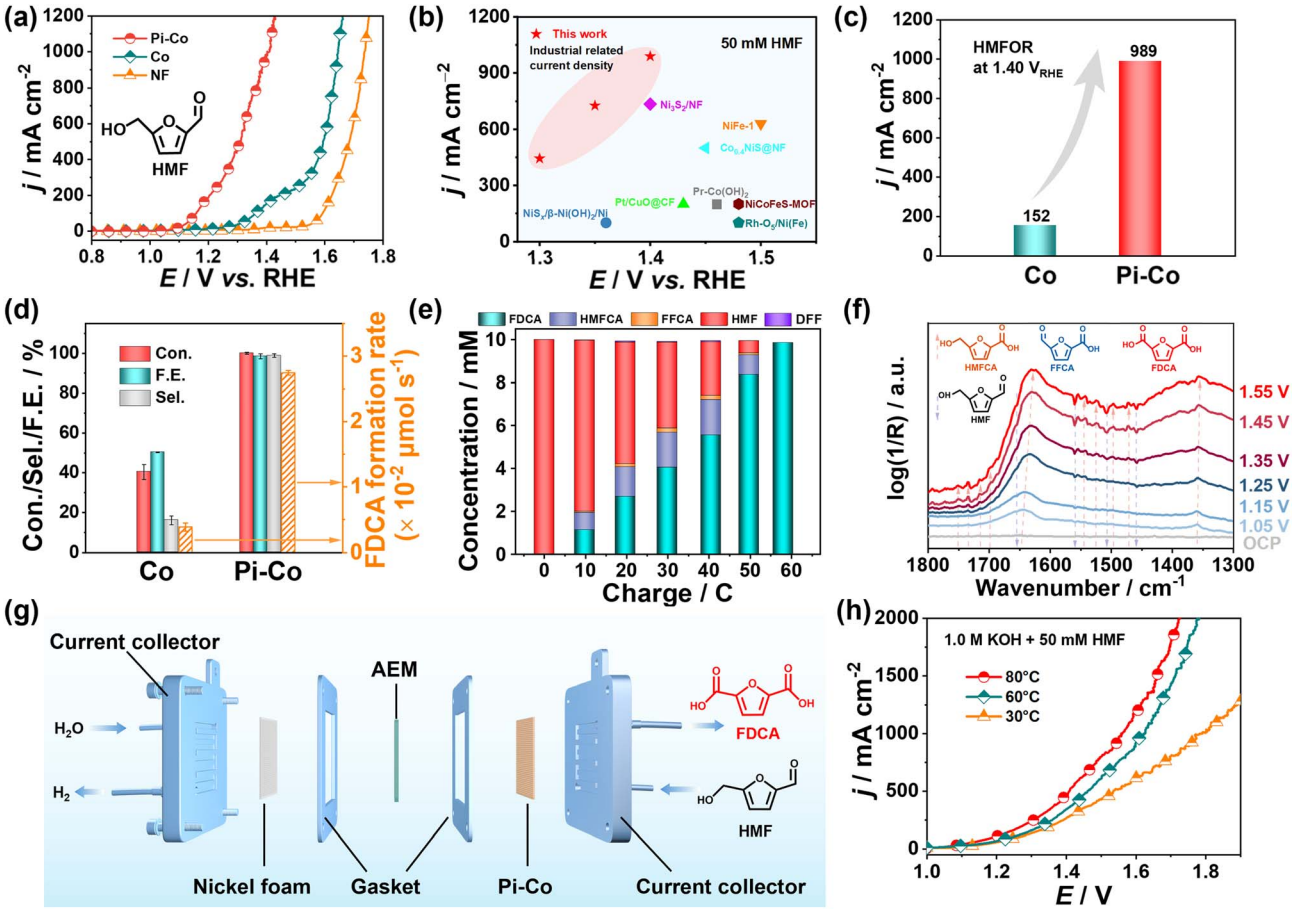

Fig. 3 (a) HMFOR LSV curves of Pi-Co and Co catalysts; (b) comparison performance with reported catalysts; (c) performance of Pi-Co and Co catalysts at 1.40 V_{RHE}; (d) HMF conversion rates of Pi-Co and Co catalysts at 1.35 V_{RHE} for 3600 s; (e) concentration changes of reaction molecules at different charges; (f) *in situ* ATR-FTIR spectra of Pi-Co catalyst at different potentials; (g) schematic diagram of the AEM-based electrolyzer and (h) the corresponding LSV curves at different temperatures.

simultaneously achieves high FDCA selectivity, formation rate, and energy conservation (Fig. S9 and S10). After electrolysis for 3600 s, the Pi-Co sample exhibits greater FDCA selectivity, faradaic efficiency (FE), and formation rate (98.8%, 98.5%, and 0.0274 μmol s^{-1}) than Co sample (16.1%, 50.3% and 0.00387 μmol s^{-1}) (Fig. 3d and S11). This suggests that the introduction of Pi leads to a significant improvement in the reaction rate and FDCA selectivity. The electrolyte could be acidified to generate a precipitate and isolate FDCA (Fig. S12), allowing for effective product separation. Additionally, Pi-Co exhibits good conversion rates, product selectivity, and FE for furfuryl alcohol (FFA) and furfural (FF) (Fig. S13), respectively, demonstrating its potential application prospects in biomass oxidation.

To elucidate the underlying reaction mechanisms, the pathways on a Pi-Co catalyst are investigated (Fig. S14 and S15). Fig. 3e and S16 illustrate that the concentration of HMFCA is consistently greater than that of 2,5-diformylfuran (DFF) throughout the electrolysis process, suggesting that the oxidation of HMF on the Pi-Co catalyst predominantly follows the HMFCA pathway. To verify this distinction, *in situ* attenuated total reflectance FTIR (ATR-FTIR) spectroscopy is employed to identify the reaction intermediates (Fig. 3f).[39] As the potential increases, the intensities of the bands at 1460, 1507, and 1558 cm^{-1} gradually decrease, whereas the intensities of the bands at 1358, 1544, 1627, and 1734 cm^{-1} increase significantly. This trend demonstrates the consumption of HMF and the simultaneous generation of 5-hydroxymethyl-2-furan carboxylic acid (HMFCA) and FDCA, confirming that the HMFOR is carried out through the HMFCA pathway.

To investigate the practical application of the Pi-Co catalyst, an anion exchange membrane (AEM)-based electrolyzer is assembled for the oxidation of HMF (Fig. 3g and S17). In this setup, Pi-Co and NF are employed as the anode and cathode respectively. For an electrolyzer with an active area of 1 cm^2 (1 × 1), the onset potential for the overall water splitting is measured at 1.50 V in a 1.0 M KOH solution at 30 °C. After adding 50 mM HMF, current densities of 500 and 1000 mA cm^{-2} are attained at potentials of 1.53 and 1.79 V (Fig. S18), respectively. Notably, when the temperature is elevated to 80 °C, the 1 cm^2 device achieves a remarkable current density of 2000 mA cm^{-2} at a potential of only 1.72 V (Fig. 3h). Additionally, the system operates stably for 70 h at a current density of 200 mA cm^{-2} while maintaining high FDCA selectivity (>90%) (Fig. S19), showing promising industrial application potential.

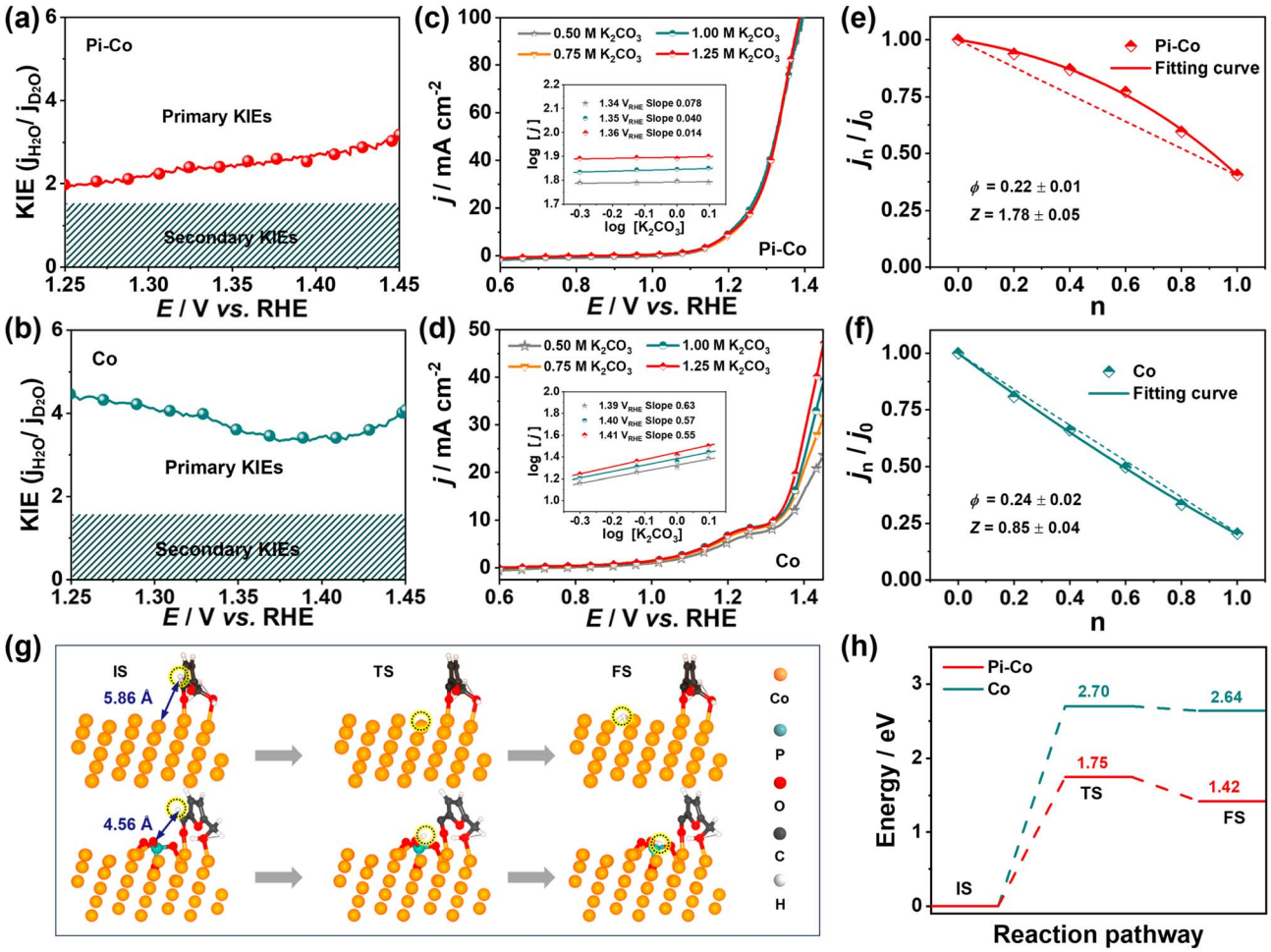

Fig. 4 (a and b) Link between the potential of Pi-Co and Co catalysts and the KIE value; (c and d) LSV curves of Pi-Co and Co catalysts in solutions with different concentrations of K_2CO_3 (pH = 13.46), the inset is the correlation between log|j| and log[K_2CO_3]; (e and f) proton inventory experiments of Pi-Co and Co catalysts: the correlation between j_n/j_0 and n; (g) initial (IS), transition (TS), and final state (FS) optimized configurations of hydrogen proton transfer from HMF to Pi-Co and Co surfaces and (h) the corresponding energy changes.

To gain insight into the structural evolution of catalysts, *in situ* Raman spectroscopy is performed at different potentials. Fig S20 reveals that both Pi-Co and Co catalysts exhibit a Co^{3+}–O peak at 503 cm^{-1} within the potential range of 1.05–1.45 V_{RHE},[40,41] indicating the formation of CoOOH during the HMFOR. The structural integrity of the Pi-Co catalyst after HMF conversion tests is also investigated (Fig. S21). SEM images show that the nanowire structure is well preserved, and its surface becomes rough (Fig. S22). XPS characterization in conjunction with Ar^+ sputtering indicate that the Co^0 peak on the surface of the Pi-Co catalyst disappears, and a new Co^{3+} peak emerges,[42,43] while the P–O peak remains prominent. When the sputtering depth reaches 5 nm, the Co^0 peak reappears, and the P–O peak almost vanishes (Fig. S23). These results indicate that the metallic Co on the surface undergoes reconstruction, while the Pi component remains basically stable in the surface, and the internal metallic Co still exists in the catalyst.

Then, to verify the effects of CoOOH on the catalytic activity of HMFOR, multi-potential step experiments are employed. The experimental procedure is as follows: first, a potential of 1.40 V_{RHE} is applied in 1.0 M KOH to generate Co^{3+} on the catalyst surface. Subsequently, HMF solution is added to the system under open-circuit potential (OCP) conditions. Finally, a reduction potential of 0.6 V_{RHE} is applied, and the change in reduction current density is monitored. Fig. S2 reveals that the chemical reaction between the activated catalyst and HMF proceeds relatively slowly below 1.40 V_{RHE} (Fig. S24(a)). In addition, electrochemical tests of the Co sample after activation show that the formation of CoOOH on the Co sample slightly improves the catalytic activity and FDCA selectivity (Fig. S24(b)). These results collectively demonstrate that CoOOH is not the key active species promoting the efficient conversion of HMF to FDCA and thus is not further discussed below.

To elucidate the internal reasons for the increase in HMFOR activity, the deuterium kinetic isotope effects (KIEs) are investigated.[44,45] When the KIEs value is greater than 1.5, it is generally regarded as clear evidence that proton transfer is involved in or affects the RDS.[18] The KIEs experiments are performed in a 1.0 M NaOD/10 mM HMF D_2O solution (Fig. S25). The Co sample has an H/D effect of 3.36–4.42 (Fig. 4a),

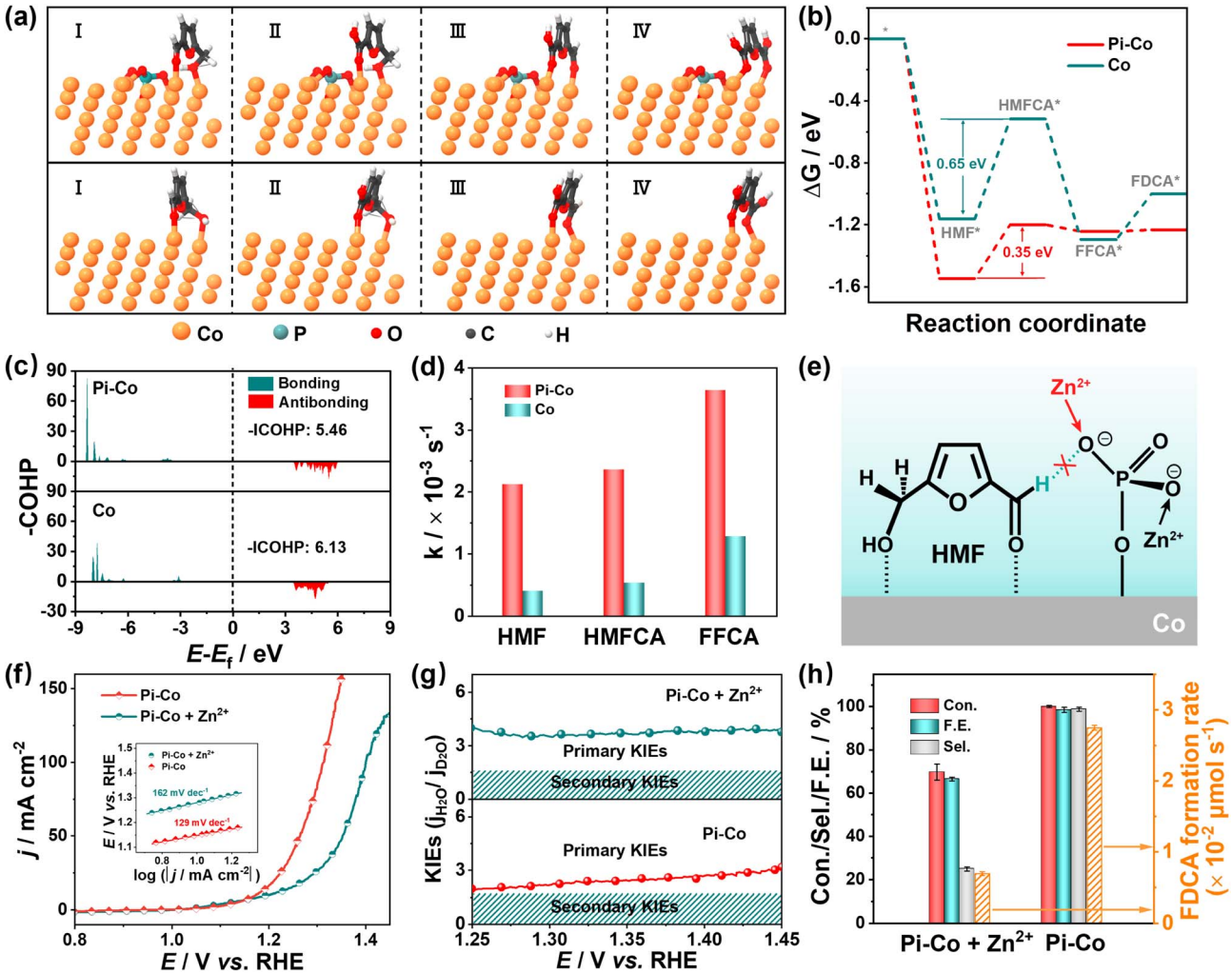

Fig. 5 (a) Optimized configurations of I HMF*, II HMFCA*, III FFCA*, and IV FDCA* on the Pi-Co and Co surfaces; (b) Gibbs free energy profiles of HMF dehydrogenation over Pi-Co and Co; (c) −COHP of the C−H bond of HMF on Pi-Co and Co; (d) reaction rate constants of HMF, HMFCA and FFCA over Pi-Co and Co; (e) schematic diagram of the interaction between Zn^{2+} and PO_4^{3-} sites of Pi-Co; (f) LSV curves and Tafel slopes (inset) of Pi-Co with/without 0.5 mmol of Zn^{2+}; (g) link between the potential of Pi-Co with/without Zn^{2+} and the KIEs value; (h) HMF conversion rate of Pi-Co with/without 0.5 mmol of Zn^{2+}.

indicating that the RDS of HMFOR over the Co sample involves C–H/O–H bond cleavage.[46] For the Pi-Co sample, the H/D effect (1.96–3.07) becomes weaker (Fig. 4b). The overlap of proton vibration wave functions plays an important role in determining the rate of proton transfer reactions and KIEs, and the degree of this overlap strongly depends on the distance between the proton donor and acceptor.[18] The smaller KIEs value of Pi-Co indicates that the Pi groups near the catalytic site shorten the proton donor–acceptor distance, thereby promoting the break of C–H/O–H bonds and improving the kinetics and selectivity of HMFOR.

When the RDS of HMFOR involves proton transfer, the Brønsted base in the solution can act as a proton acceptor to reduce the energy barrier of the reaction, affecting the overall reaction kinetics.[47,48] The relationships between the catalytic activities of the Pi-Co and Co samples and the concentration of the additional base (K_2CO_3) are studied. As shown in Fig. 4c and d, the current density of the Co sample increases with K_2CO_3 concentration increasing, whereas the activity of Pi-Co is nearly unaffected. In addition, the additional base order of Pi-Co (0.04) is significantly smaller than that of the Co sample (0.57) (Fig. 4c and d inset), indicating that the proton transfer process in the additional base solution is inhibited. This is because the proton affinity of the phosphate group is greater than the carbonate group, which effectively offsets the deprotonation of K_2CO_3 in the electrolyte and greatly improves the efficiency of proton transfer on the catalyst surface. These results demonstrate that the Pi groups, as efficient carriers of proton transfer, accelerate the proton transfer kinetics of HMFOR.

To gain a deeper understanding of the promotional effect of Pi on proton transfer, an electrochemical proton inventory study is conducted. This method explores the number of exchangeable hydrogen sites and their impact on proton transfer kinetics by measuring the reaction rate as a function of

D_2O concentration in a D_2O/H_2O mixed solvent (Fig. S26).[49,50] Fig. 4e reveals that the Pi-Co sample exhibits a distinct nonlinear arc pattern with a large Z value (1.78) and a small ϕ value (0.22). This finding indicates that the Pi groups improve the efficiency of proton transfer by providing additional equivalent hydrogen sites, which is closely related to the polymer reverse isotope effect in the RDS. In contrast, the Co sample without the Pi groups has a smaller Z value (0.85) and a slightly larger ϕ value (0.24) (Fig. 4f) and has a negligible effect on the proton transfer kinetics. These findings suggest that Pi groups affect proton transfer in the RDS through their equivalent hydrogen sites, thereby improving the proton transfer efficiency of the Co catalytic center.

The proton transfer energy barrier in the step of HMF dehydrogenation on Co and Pi-Co surfaces is further investigated *via* DFT simulations (Fig. 4g). For the Co sample, the hydrogen proton in the HMF is transferred to the Co site. However, after the introduction of the Pi groups, the hydrogen proton is preferentially transferred to the O position of Pi. This leads to a reduction in the proton donor–acceptor distance from 5.86 Å for Co to 4.56 Å for Pi-Co. Consequently, the energy barrier for proton transfer from the HMF molecule to the surfaces of Co and Pi-Co is significantly decreased from 2.70 eV to 1.75 eV (Fig. 4h). This confirms that the introduction of Pi shortens the distance between the proton donor and acceptor and promotes the proton transfer kinetics during the dehydrogenation of HMF.

The specific reaction process of HMFOR is studied to reveal the RDS step of the dehydrogenation of HMF to FDCA (Fig. 5a). The calculated results indicate that the RDS of both the Pi-Co and Co samples are the dehydrogenation of HMF* to HMFCA* (Fig. 5b). For the Co sample, the Gibbs free energy for the formation of HMFCA* is 0.65 eV. The presence of Pi on the Co surface significantly decreases the Gibbs free energy for HMFCA* (0.35 eV), suggesting that introducing Pi on the Co surface is more energetically favorable for the dehydrogenation process. To elucidate the mechanism underlying this phenomenon, the adsorption energies of key reactant molecules are calculated. The results reveal that the adsorption energy of HMF* on Pi-Co (−2.29 eV) is significantly negative than that on Co (−1.61 eV) (Fig. S27), demonstrating that Pi functionalization effectively enhances the adsorption of HMF. Furthermore, crystal orbital Hamilton population (COHP)[51] calculations show that the –ICOHP value of the C–H bond on the Co sample (6.13) is more positive than that on Pi-Co (5.46) (Fig. 5c), suggesting a relatively weak C–H strength of HMF* on Pi-Co. These results indicate that the introduction of Pi promotes the adsorption of the reaction molecules and the break of the C–H bonds in the RDS process, which is beneficial for improving the kinetics and selectivity of HMFOR.

The oxidation rate constants of HMF, HMFCA, and FFCA over the catalysts are examined to validate the RDS (Fig. S28).[52] Fig. 5d shows that the rate constant of HMF is significantly lower than those of HMFCA and FFCA, confirming that the RDS is the conversion of HMF to HMFCA. Notably, the HMF, HMFCA, and FFCA rates of Pi-Co are 5.33, 4.43, and 2.84 times greater than Co sample, respectively, further demonstrating that the introduction of Pi groups improves the reaction rates and optimizes the RDS during HMFOR.

Furthermore, to obtain additional evidence for the vital role of Pi during HMF oxidation, zinc ions (Zn^{2+}) are introduced into the solution to block the surface Pi groups through strong interactions between the Zn^{2+} and PO_4^{3-} sites (Fig. 5e).[53] Fig. 5f and the inset reveal a notable decrease in the current density and an increase in the Tafel slope after the addition of Zn^{2+}. KIEs experiments show that the current density of the Pi-Co blocked with Zn^{2+} decreases, and the H/D effect increases to 3.48–4.02 (Fig. 5g and S29), demonstrating that interfacial proton transfer is inhibited when surface Pi sites are blocked. HMF conversion tests indicate that the FDCA selectivity, FE, and formation rate significantly decrease to 24.0%, 66.5%, and 0.00691 μmol s^{-1} (Fig. 5h and S30), respectively. These findings provide further evidence for the crucial role of surface Pi species in promoting HMF oxidation.

Conclusions

In summary, this work enhances the interfacial proton transfer between the catalyst and the reactant molecules by functionalizing Co nanowires with Pi groups. The Pi-functionalized catalyst significantly enhances the HMFOR performance, reaction rate, and FDCA selectivity. Computational and experimental methods demonstrate that the ease of proton transfer plays an important role in the RDS of dehydrogenation during the HMFOR process, and the introduction of Pi groups on the Co surface facilitates proton transfer from the reaction molecules to the surface of the catalyst to achieve rapid dehydrogenation, thereby improving the reaction kinetics and product selectivity. This study provides an understanding of the key role played by the proton transfer process in biomass electrooxidation, thus facilitating the development of efficient electrocatalytic refining catalysts.

Author contributions

J. W. designed the work, planned the experiments, and drafted the initial manuscript. J. Z. and Z. Z. conducted the theoretical calculations. Z. S., Z. Z., J. C., and Z. N. carried out the characterization experiments. H. W. and S. Y. supervised the research and contributed to the review and editing of the manuscript. All authors participated in discussions and revised the manuscript.

Conflicts of interest

There are no conflicts to declare.

Data availability

All data included in this study are available upon request by contact with the corresponding author.

Supplementary information is available. See DOI: **https://doi.org/10.1039/d5sc04035c**.

Acknowledgements

This work is supported by the National Natural Science Foundation of China (22479031, 22162004), the Natural Science Foundation of Guangxi (2022JJD120011), and the High-Performance Computing Platform of Guangxi University.

References

1 C. Tang, Y. Zheng, M. Jaroniec and S. Z. Qiao, Electrocatalytic refinery for sustainable production of fuels and chemicals, *Angew. Chem., Int. Ed.*, 2021, **60**, 19572–19590.
2 X. L. Liu, W. Zhong, Y. F. Jin, T. J. Wang, X. Xiao, P. Chen, Y. Chen and X. Ai, Pd–Pt bimetallene for the energy-saving electrochemical hydrogenation of 5-hydroxymethylfurfural, *Chin. J. Catal.*, 2025, **69**, 241–248.
3 Z. Wang, Q. L. Hong, B. Q. Miao, T. J. Wang, Y. Ding, P. J. Jin, P. Chen and Y. Chen, Organic interfacial engineering of gold nanowires for selective glycerol electrooxidation, *Chin. Chem. Lett.*, 2024, **35**, 108458.
4 N. C. Luo, T. Montini, J. Zhang, P. Fornasiero, E. Fonda, T. T. Hou, W. Nie, J. M. Lu, J. X. Liu and M. Heggen, Visible-light-driven coproduction of diesel precursors and hydrogen from lignocellulose-derived methylfurans, *Nat. Energy*, 2019, **4**, 575–584.
5 J. W. Zhang, P. L. Yu, G. M. Zeng, F. X. Bao, Y. L. Yuan and H. W. Huang, Boosting HMF oxidation performance via decorating ultrathin nickel hydroxide nanosheets with amorphous copper hydroxide islands, *J. Mater. Chem. A*, 2021, **9**, 9685–9691.
6 P. Zhou, X. S. Lv, S. S. Tao, J. C. Wu, H. F. Wang, X. X. Wei, T. H. Wang, B. Zhou, Y. X. Lu, T. Frauenheim, X. Z. Fu, S. Y. Wang and Y. Q. Zou, Heterogeneous-interface-enhanced adsorption of organic and hydroxyl for biomass electrooxidation, *Adv. Mater.*, 2022, **34**, 2204089.
7 P. H. Xu, Z. Y. Bao, Y. J. Zhao, L. X. Zheng, Z. Q. Lv, X. W. Shi, H. E. Wang, X. S. Fang and H. J. Zheng, Anionic regulation and heteroatom doping of Ni-based electrocatalysts to boost biomass valorization coupled with hydrogen production, *Adv. Energy Mater.*, 2024, **14**, 2303557.
8 X. P. Liu, X. H. Wang, C. X. Mao, J. Y. Qiu, R. Wang, Y. Liu, Y. Chen and D. L. Wang, Ligand-hybridization activates lattice-hydroxyl-groups of $NiCo(OH)_x$ nanowires for efficient electrosynthesis, *Angew. Chem., Int. Ed.*, 2024, **63**, e202408109.
9 G. H. Ding, H. Lee, X. Cao, Z. H. Li, J. B. Liu, L. Q. Wang, Y. X. Ding, L. Q. Yin and L. C. Sun, 5-Hydroxymethylfurfural oxidation in scaled anion exchange membrane electrolyzer with $NiCuO_x$ catalyst, *ACS Energy Lett.*, 2025, **10**, 571–578.
10 J. Wu, J. L. Chen, T. Q. Yu, Z. X. Zhai, Y. M. Zhu, X. Z. Wu and S. B. Yin, Boosting electrochemical kinetics of $NiCo_2$ via MoO_2 modification for biomass upgrading assisted hydrogen evolution, *ACS Catal.*, 2023, **13**, 13257–13266.
11 J. F. Zhang, Y. Shen, Z. L. Wu, X. Y. Zhang, J. Kang, Y. J. Wu, S. B. Zhang, S. Chen, G. Z. Wang and H. M. Zhang, Efficient alkaline-free electrooxidation of 5-hydroxymethylfurfural to 2,5-furandicarboxylic acid using electrochemically-charged $Ni_xCo_{1-x}(OH)_2$ as a redox mediator, *Angew. Chem., Int. Ed.*, 2025, e202423109.
12 L. Chen, C. Yu, X. D. Song, J. T. Dong, J. W. Mu and J. S. Qiu, Integrated electrochemical and chemical system for ampere-level production of terephthalic acid alternatives and hydrogen, *Nat. Commun.*, 2024, **15**, 8072.
13 M. F. Li, S. L. Hu, Y. C. Zhang, J. N. Qin, D. Y. Min, C. L. Chen, P. J. Zhang, L. Q. Jiang and J. Zhang, Regulation of oxygen vacancy in Mn-Co oxides to enhance selective oxidation of 5-hydroxymethylfurfural to 2,5-furandicarboxylic acid, *Appl. Catal., B*, 2025, **368**, 125130.
14 J. Wu, Z. X. Zhai, S. B. Yin and S. Y. Wang, General formation of interfacial assembled hierarchical micro-nano arrays for biomass upgrading-coupled hydrogen production, *Adv. Funct. Mater.*, 2024, **34**, 2308198.
15 H. L. Dai, Y. F. Huang, H. Y. Bai, H. P. Li, H. Q. Zhao, F. G. Wang, W. Q. Fan and W. D. Shi, Adsorption–activation bifunctional center of Al/Co-base catalyst for boosting 5-hydroxymethylfurfural oxidation, *Adv. Energy Mater.*, 2024, **14**, 2402789.
16 X. Peng, X. Jin, B. Gao, Z. T. Liu and P. K. Chu, Strategies to improve cobalt-based electrocatalysts for electrochemical water splitting, *J. Catal.*, 2021, **398**, 54–66.
17 Y. C. Yang and T. C. Mu, Electrochemical oxidation of biomass derived 5-hydroxymethylfurfural (HMF): pathway, mechanism, catalysts and coupling reactions, *Green Chem.*, 2021, **23**, 4228–4254.
18 W. L. Li, F. S. Li, H. Yang, X. J. Wu, P. L. Zhang, Y. Shan and L. C. Sun, A bio-inspired coordination polymer as outstanding water oxidation catalyst *via* second coordination sphere engineering, *Nat. Commun.*, 2019, **10**, 5074.
19 M. T. Zhang, T. Irebo, O. Johansson and L. Hammarstrom, Proton-coupled electron transfer from tyrosine: a strong rate dependence on intramolecular proton transfer distance, *J. Am. Chem. Soc.*, 2011, **133**, 13224–13227.
20 T. Wang, Y. R. Zhang, B. T. Huang, B. Cai, R. R. Rao, L. Giordano, S. G. Sun and Y. Shao Horn, Enhancing oxygen reduction electrocatalysis by tuning interfacial hydrogen bonds, *Nat. Catal.*, 2021, **4**, 753–762.
21 M. K. Ludlow, A. V. Soudackov and S. Hammes Schiffer, Electrochemical proton-coupled electron transfer of an osmium aquo complex: theoretical analysis of asymmetric Tafel plots and transfer coefficients, *J. Am. Chem. Soc.*, 2010, **132**, 1234–1235.
22 R. Tyburski, T. Liu, S. D. Glover and L. Hammarström, Proton-coupled electron transfer guidelines, fair and square, *J. Am. Chem. Soc.*, 2021, **143**, 560–576.
23 G. B. Kauffman, The Bronsted–Lowry acid base concept, *J. Chem. Educ.*, 1988, **65**, 28.
24 C. Z. Yang, C. Laberty Robert, D. Batuk, G. Cibin, A. V. Chadwick, V. Pimenta, W. Yin, L. Zhang, J. M. Tarascon and A. Grimaud, Phosphate ion functionalization of perovskite surfaces for enhanced oxygen evolution reaction, *J. Phys. Chem. Lett.*, 2017, **8**, 3466–3472.

25 B. M. Hunter, W. Hieringer, J. Winkler, H. Gray and A. Müller, Effect of interlayer anions on [NiFe]-LDH nanosheet water oxidation activity, *Energy Environ. Sci.*, 2016, **9**, 1734–1743.

26 X. F. Zhu, Y. Ding, S. N. Li, Y. C. Jiang and Y. Chen, Electroenzymatic cascade reaction on a biohybrid boosts the chiral epoxidation reaction, *Sci. Bull.*, 2024, **69**, 483–491.

27 X. Shi, A. P. Wu, H. J. Yan, L. Zhang, C. G. Tian, L. Wang and H. G. Fu, A "MOFs plus MOFs" strategy toward Co–Mo_2N tubes for efficient electrocatalytic overall water splitting, *J. Mater. Chem. A*, 2018, **6**, 20100–20109.

28 H. Xu, G. X. Xu, L. S. Chen and J. L. Shi, Self-Co-electrolysis for Co-production of phosphate and hydrogen in neutral phosphate buffer electrolyte, *Adv. Mater.*, 2022, **34**, 2200058.

29 H. Yan, M. Y. Zhao, X. Feng, S. M. Zhao, X. Zhou, S. F. Li, M. H. Zha, F. Y. Meng, X. B. Chen and Y. B. Liu, PO_4^{3-} coordinated robust single-atom platinum catalyst for selective polyol oxidation, *Angew. Chem., Int. Ed.*, 2022, **134**, e202116059.

30 A. Indra, P. W. Menezes, I. Zaharieva, H. Dau and M. Driess, Detecting structural transformation of cobalt phosphonate to active bifunctional catalysts for electrochemical water-splitting, *J. Mater. Chem. A*, 2020, **8**, 2637–2643.

31 B. T. Fan, H. Zhang, B. Gu, F. Qiu, Q. Cao and W. H. Fang, Constructing Pr-doped CoOOH catalytic sites for efficient electrooxidation of 5-hydroxymethylfurfural, *J. Energy Chem.*, 2025, **100**, 234–244.

32 C. F. Liu, X. R. Shi, K. H. Yue, P. J. Wang, K. Zhan, X. Y. Wang, B. Y. Xia and Y. Yan, S-species-evoked high-valence $Ni^{2+\delta}$ of the evolved β-$Ni(OH)_2$ electrode for selective oxidation of 5-hydroxymethylfurfural, *Adv. Mater.*, 2023, **35**, 2211177.

33 J. R. Li, R. X. Qiu, S. W. Zhang, L. Peng, Y. Y. Dong, Y. Jiang, Y. Li, N. Fang, J. Yu and J. C. Dong, Synergistically enhanced Co-adsorption of reactant and hydroxyl on platinum-modified copper oxide for high-performance HMF oxidation, *Adv. Mater.*, 2025, 2417684.

34 L. Chen, Z. H. Yang, C. Y. Yan, Y. J. Yin, Z. M. Xue, Y. T. Yao, S. Wang, F. F. Sun and T. C. Mu, Modulating Ni–S coordination in Ni_3S_2 to promote electrocatalytic oxidation of 5-hydroxymethylfurfural at ampere-level current density, *Chem. Sci.*, 2024, **15**, 12047–12057.

35 Y. Sun, J. Wang, Y. F. Qi, W. J. Li and C. Wang, Efficient electrooxidation of 5-hydroxymethylfurfural using Co-doped Ni_3S_2 catalyst: Promising for H_2 production under industrial-level current density, *Adv. Sci.*, 2022, **9**, 2200957.

36 L. Y. Zeng, Y. J. Chen, M. Z. Sun, Q. Z. Huang, K. A. Sun, J. Y. Ma, J. Li, H. Tan, M. G. Li and Y. Pan, Cooperative Rh-O_5/Ni(Fe) site for efficient biomass upgrading coupled with H_2 production, *J. Am. Chem. Soc.*, 2023, **145**, 17577–17587.

37 C. L. Wang, Y. F. Wu, A. Bodach, M. L. Krebs, W. Schuhmann and F. Schüth, A novel electrode for value-generating anode reactions in water electrolyzers at industrial current densities, *Angew. Chem., Int. Ed.*, 2023, **62**, e202215804.

38 Y. X. Feng, K. Yang, R. L. Smith and X. H. Qi, Metal sulfide enhanced metal–organic framework nanoarrays for electrocatalytic oxidation of 5-hydroxymethylfurfural to 2, 5-furandicarboxylic acid, *J. Mater. Chem. A*, 2023, **11**, 6375–6383.

39 S. Barwe, J. Weidner, S. Cychy, D. M. Morales, S. Dieckhöfer, D. Hiltrop, J. Masa, M. Muhler and W. Schuhmann, Electrocatalytic oxidation of 5-(hydroxymethyl) furfural using high-surface-area nickel boride, *Angew. Chem., Int. Ed.*, 2018, **57**, 11460–11464.

40 Y. F. Zhou, Y. Shen and H. Y. Li, Mechanistic study on electro-oxidation of 5-hydroxymethylfurfural and water molecules via operando surface-enhanced Raman spectroscopy coupled with an Fe^{3+} probe, *Appl. Catal., B*, 2022, **317**, 121776.

41 X. H. Deng, G. Y. Xu, Y. J. Zhang, L. Wang, J. J. Zhang, J. F. Li, X. Z. Fu and J. L. Luo, Understanding the Roles of Electrogenerated Co^{3+} and Co^{4+} in Selectivity-Tuned 5-Hydroxymethylfurfural Oxidation, *Angew. Chem., Int. Ed.*, 2021, **133**, 20698–20705.

42 C. M. Lou, K. Wang, X. H. Liu, X. Y. Li, H. Wang, L. H. Li, W. Zheng and J. Zhang, Heterogeneous Co_3O_4/carbon nanofibers for low temperature triethylamine detection: mechanistic insights by operando DRIFTS and DFT, *Adv. Mater. Interfaces*, 2022, **9**, 2101479.

43 Z. C. Jia, Y. Yuan, Y. X. Zhang, X. Lyu, C. H. Liu, X. L. Yang, Z. Y. Bai, H. J. Wang and L. Yang, Optimizing 3d spin polarization of CoOOH by in situ Mo doping for efficient oxygen evolution reaction, *Carbon Energy*, 2024, **6**, e418.

44 H. Yamada, W. F. Siems, T. Koike and J. K. Hurst, Mechanisms of water oxidation catalyzed by the cis, cis-$[(bpy)_2Ru(OH_2)]_2O^{4+}$ ion, *J. Am. Chem. Soc.*, 2004, **126**, 9786–9795.

45 N. K. Roberts and H. L. Northey, Proton and deuteron mobility in normal and heavy water solutions of electrolytes, *J. Am. Chem. Soc.*, 1974, **70**, 253–262.

46 M. Gómez Gallego and M. A. Sierra, Kinetic isotope effects in the study of organometallic reaction mechanisms, *Chem. Rev.*, 2011, **111**, 4857–4963.

47 Z. F. Chen, A. K. Vannucci, J. J. Concepcion, J. W. Jurss and T. J. Meyer, Proton-coupled electron transfer at modified electrodes by multiple pathways, *Proc. Natl. Acad. Sci. U. S. A.*, 2011, **108**, E1461–E1469.

48 Y. Zhang, H. Zhang, H. Ji, W. Ma, C. Chen and J. Zhao, Pivotal role and regulation of proton transfer in water oxidation on hematite photoanodes, *J. Am. Chem. Soc.*, 2016, **138**, 2705–2711.

49 P. F. Fitzpatrick, Combining solvent isotope effects with substrate isotope effects in mechanistic studies of alcohol and amine oxidation by enzymes, *Biochim. Biophys. Acta, Proteins Proteomics*, 2015, **1854**, 1746–1755.

50 Y. S. Liu and C. C. McCrory, Modulating the mechanism of electrocatalytic CO_2 reduction by cobalt phthalocyanine through polymer coordination and encapsulation, *Nat. Commun.*, 2019, **10**, 1683.

51 L. S. Qiu, G. K. Zheng, Y. He, L. C. Lei and X. W. Zhang, Ultra-small Sn-RuO_2 nanoparticles supported on N-doped carbon polyhedra for highly active and durable oxygen evolution reaction in acidic media, *Chem. Eng. J.*, 2021, **409**, 128155.

52 H. L. Wang, Y. M. Zhou and S. Y. Tao, CoP-CoOOH heterojunction with modulating interfacial electronic structure: a robust biomass-upgrading electrocatalyst, *Appl. Catal., B*, 2022, **315**, 121588.

53 W. Shin, J. Lee, Y. Kim, H. Steinfink and A. Heller, Ionic conduction in $Zn_3(PO_4)_2 \cdot 4H_2O$ enables efficient discharge of the zinc anode in serum, *J. Am. Chem. Soc.*, 2005, **127**, 14590–14591.